Chapter 2

METHODOLOGY: MULTI-SOURCEDNESS

> *"The extra dimension seems to make a lot of difference. But if a little bit of gauge freedom is this good, what would a lot of it be like? Could fluid dynamics, even turbulence, appear simple when viewed in a space of (say) 26 dimensions?"*
>
> – Rick Salmon, *More Lectures on Geophysical Fluid Dynamics*

The purpose of wind tunnels, most discernibly, is to *generate wind* and their utility must then be derived from their capacity to simulate a proper environment. While even the most capable wind tunnel facilities are tunably adapted to generating high velocity flows, they are generally limited in the types of flows they can produce. In contrast, a multi-source wind tunnel is capable of generating a host of spatiotemporally-varying flows subject to the size, number, and responsiveness of the base source unit. When coupled in-phase, the multi-source wind tunnel serves equivalent to a conventional wind tunnel, provided the flow is given enough downstream distance to homogenize. For a fixed outer dimension, the design trade-off essentially amounts to one of temporal responsiveness (i.e. smaller source units would require less inertia to rotate) and overall complexity (i.e. one base unit to operate versus many). In this chapter, a mathematical framework to describe the basic characteristics of a multi-source flow-generating apparatus is introduced. Then, the downstream evolution of the baseline steady uniform flow modality is presented followed by brief discussions of the unsteady and quasi-steady counterparts.

2.1 Experimental premise: multi-sourcedness

When source units are assembled into an array, two primary benefits emerge. First, flow characteristics are initialized at the base unit scale thus reducing the overall mixing length of source-related turbulence, particularly useful in space-constrained[1] implementations. Secondly, the ability to generate spatially-varying flowfields without the need to introduce obstacle geometries downstream affords a convenience to explore greater flow varieties for a given experimental setup all the while preserving the potential for free-flight testing. The source unit of each of the multi-source wind tunnels used herein is a DC-powered off-the-shelf cooling fan that is assembled into an array either individually or through a sub-module of nine units arranged in a square 3x3 configuration. These so-called fan array wind tunnels (FAWT) developed within the Graduate Aerospace Laboratory at Caltech (GALCIT) comprise a sub-class of multi-source wind tunnels and are described in great detail in appendix A. For the purposes herein, a theoretical treatment of the source unit is provided to inform expected performance bounds when designing flowfields to be considered as candidates for environmental forcing spectra that simulate atmospheric-like disturbances in regions of interest.

The fan source unit

The most basic building block of a fan array wind tunnel is the source fan unit itself, typically described by its outer dimension, d.

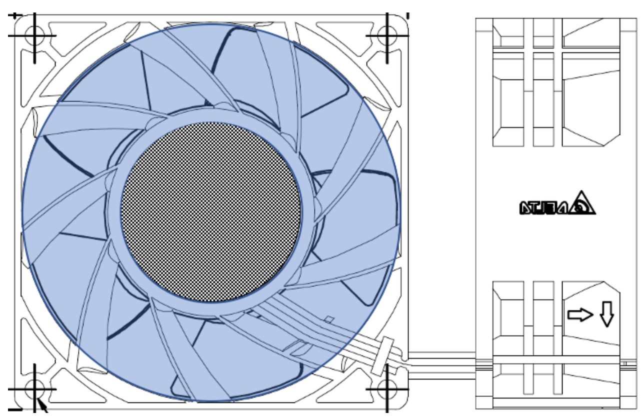

Figure 2.1: Schematic of the basic type fan unit typically used in FAWT. The part highlighted in blue represents the annular flow output area. Arrays built from the fan unit as diagrammed constitute a single-layer fan array. A dual-layer fan array is comprised of counter-rotating pairs of stacked single fan units that do not change the overall footprint but increase the depth by one stacked layer. These dual-layer fan arrays can be coupled front-and-back layer or remain individually controllable.

Flow is initiated at the scale of the fan unit, emanating out of an annular fan outlet plane, marked in blue in fig. 2.1. Measurements of the streamwise evolution of the flow suggest (see fig. A.4) that the incompressible flow is fully mixed beyond $x/d \gtrsim 20$, whereby the flow has achieved its nominal velocity expanding from an initial fan annular area, A_{ann}, to an equivalent area, A_{eq}, governed by eq. (1.2), that is roughly the size of the outer geometric dimensions of the fan unit itself (i.e. $d \times d$). The flow is driven by a pressure gradient across the fan blades that is typically

[1]If there exists no space-constraint, than any single-source wind tunnel can be made proportionately bigger by adding more sources and would thus classify as a multi-source wind tunnel.

provided by a manufacturer specification sheet in the form of a 'p-Q curve' — a plot of the static pressure, p, as a function of volumetric flow rate, Q.

Applying the fundamentals

For an incompressible, irrotational[2], inviscid (i.e. $Re \to \infty$) non-steady, constant density flowfield in the absence of changing external body forces (i.e. $Fr \to \infty$), eq. (1.7) reduces to:

$$[St]\frac{\partial \underline{u}^*}{\partial t^*} + \nabla^*(\frac{1}{2}\underline{u}^* \cdot \underline{u}^*) \; = \; -[Eu]\nabla^* p^* \tag{2.1}$$

Recalling table 1.1, and taking the characteristic length as $L = ds$, where ds is an increment along a streamline, and the characteristic velocity $U = \overline{u}$ to be the mean velocity of the flowfield, eq. (2.1) can be written as:

$$\frac{1}{\overline{u}}\frac{\partial \underline{u}^*}{\partial t}\; ds + \frac{1}{2}\nabla(\underline{u}^* \cdot \underline{u}^*)\; ds \; = \; -\frac{1}{\rho\overline{u}^2}\nabla p\; ds \tag{2.2}$$

where the scaled instantaneous velocity remains $\underline{u}^* = \underline{u}/\overline{u}$. Restricting the view to changes that occur along a given streamline gives:

$$\frac{1}{\overline{u}}\frac{\partial \underline{u}^*}{\partial t}\; ds + \frac{1}{2}d(\underline{u}^{*^2}) \; = \; -\frac{1}{\rho\overline{u}^2}\; dp \tag{2.3}$$

Integrating from the inlet (subscript i) to the test section exit plane (subscript e) yields:

$$\frac{1}{\overline{u}}\int_i^e \frac{\partial \underline{u}^*}{\partial t}\; ds + \frac{1}{2}(\underline{u}_e^{*^2} - \underline{u}_i^{*^2}) = -\frac{1}{\rho\overline{u}^2}\;(p_e - p_i) \tag{2.4}$$

which is a form of the unsteady Bernoulli's equation along a streamline.

In diagram form, it is recognized that the manufacturer provided specifications are valid at the fan inlet plane; velocity calibration measurements, however, are taken (well-) beyond $x \gtrsim 20d$, denoted by subscript ∞ to imply centerline freestream measurements. For the one-dimensional flow considered here (i.e. $\underline{u} = \{u, 0, 0\}$), the volumetric flow rate across the inlet and outlet planes is:

$$Q = u_{ann}A_{ann} = u_\infty A_{eq} \tag{2.5}$$

which through the area ratio (A_{eq}/A_{ann}) allows for the analysis to deal solely with the freestream velocity, u_∞, measured beyond the initial mixing zone. Given the

[2]For irrotational flow, $(\nabla \times \underline{u}) = 0$, such that $(\underline{u} \cdot \nabla)\underline{u} = \frac{1}{2}\nabla(\underline{u} \cdot \underline{u})$. A swirl-free assumption for counter-rotating dual-unit fans without a honeycomb is reasonably met in some cases but is certainly applicable to both single- and dual-unit fans with a honeycomb installed for a uniform flow modality.

assumptions, for a uniform flow modality, the analysis extends to $n-$fan units, with proportional changes in volumetric flow rate (nQ) resulting in proportionally bigger reference areas (i.e. nA_{ann} and nA_{eq}) that ultimately reduce to eq. (2.5). The static pressure across the inlet does not change with increasing n when fan units are stacked parallel to one another.

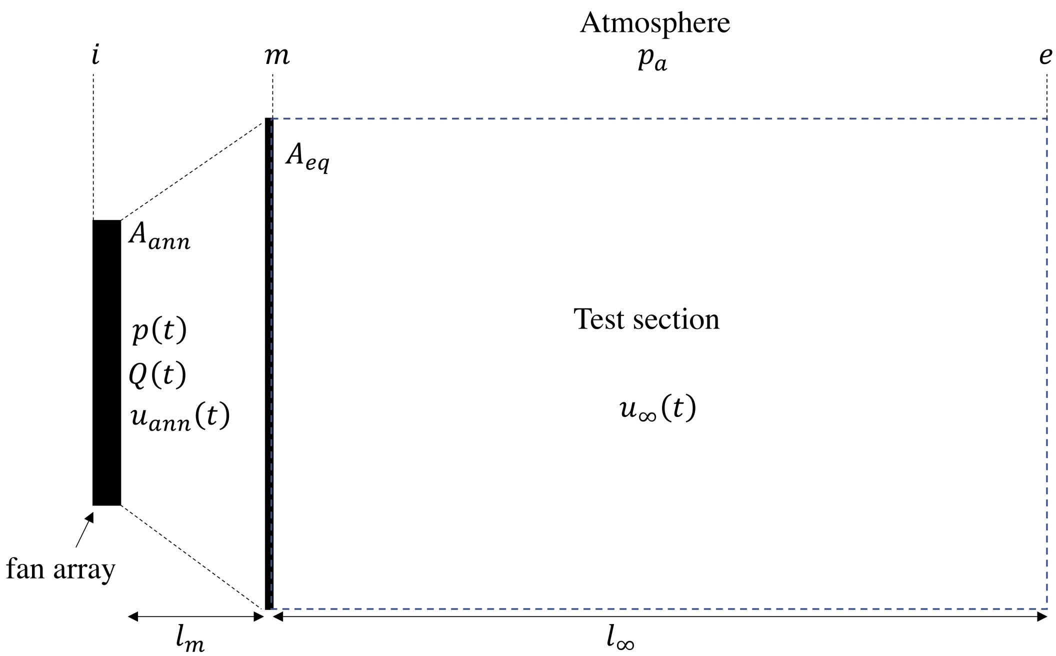

Figure 2.2: Control volume schematic for FAWT analysis.

Frequency bandwidth

The analysis can be further extended to an oscillating (or fluctuating) component of the velocity field, taken to be $\tilde{u}$, provided that, on average, $\overline{\tilde{u}} = 0$. The decomposition then is written as $\underline{u} = \overline{u} + \tilde{u}$, which yields:

$$\underline{u}^* = \frac{\overline{u} + \tilde{u}}{\overline{u}} = \frac{\overline{u}}{\overline{u}} + \frac{\tilde{u}}{\overline{u}} = 1 + \widetilde{u^*} \tag{2.6}$$

The pressure and volumetric flow rate can likewise be decomposed into a time-averaged[3]and unsteady component, as in (Greenblatt, 2016), to collectively give:

$$\underline{u}^*(t) = 1 + \widetilde{u^*}(t) \tag{2.7}$$

$$p(t) = \overline{p} + \widetilde{p}(t) \tag{2.8}$$

$$Q(t) = \overline{Q} + \widetilde{Q}(t) \tag{2.9}$$

In accordance with fig. 2.2 (i.e. $\underline{u} = \{u_\infty, 0, 0\}$), $\underline{u}^*(t)$ is written as:

$$\underline{u}^*(t) = 1 + \frac{\tilde{u}_\infty(t)}{U_\infty} = 1 + \tilde{u}^*_\infty(t) \tag{2.10}$$

Inserting eq. (2.10) and eq. (2.8) into eq. (2.4) with the inlet velocity taken to be nearly zero (i.e. $\underline{u_i}^{*^2} \approx 0$) at atmospheric pressure, p_a, and time-averaging, after rearrangement yields:

$$U_\infty = \sqrt{\frac{2\Delta p}{\rho} - \overline{\tilde{u}^2_\infty}} \tag{2.11}$$

where $\Delta p \equiv p_a - \overline{p}$. When $\overline{\tilde{u}^2_\infty} << U^2_\infty$, eq. (2.11) recovers the freestream velocity expression of the steady form of the Bernoulli equation.

The equation governing the motion of the fluctuating components is derived by subtracting the time-averaged form from the instantaneous form to yield:

$$\frac{L_t}{U_\infty}\frac{\partial \tilde{u}^*_\infty}{\partial t} + \tilde{u}^*_\infty = -\frac{\tilde{p}(t)}{\rho {U_\infty}^2} - \frac{1}{2}(\tilde{u}^{*^2}_\infty - \overline{\tilde{u}^{*^2}_\infty}) \tag{2.12}$$

The linearized form (i.e. ignoring the rightmost higher order terms) of eq. (2.12) gives an expression of the form $\tau\, \tilde{u}^{*'}_\infty + \tilde{u}^*_\infty = g(t)$, which is a forced first order linear differential equation with time constant $\tau = 1/2\pi f_c = L_t/U_\infty$. The cutoff frequency, f_c is then:

$$f_c = \frac{1}{2\pi\tau} = \frac{1}{2\pi}\frac{U_\infty}{L_t} \tag{2.13}$$

For a sinusoidal forcing function of the form $\tilde{p} = A\sin(\omega t)$, eq. (2.12) can be solved numerically. When linearized, the analytical solution is:

$$\tilde{u}^*_\infty(t) = B\sin(\omega t + \phi) \tag{2.14}$$

where $M = B/A = \sqrt{1 + \omega^2\tau^2}$ is the magnitude gain ratio and $\phi = -\tan^{-1}\omega t$ is the phase delay. Treated this way, beyond the initial mixing region, the system behaves as a low-pass filter and the air moves as a lumped mass phase-delayed by ϕ with a magnitude response governed by M for a given frequency, $\omega = 2\pi f$.

The characteristic length $L_t = L_m + L_\infty$ is not well-defined due to a lack of measurement data far downstream of open-jet wind tunnels. The theoretical treatment herein suggests L_t is of the order 10^1, with an example given in fig. 2.3.

[3] in the case of an oscillation, the time-average is taken as integration over an oscillation period.

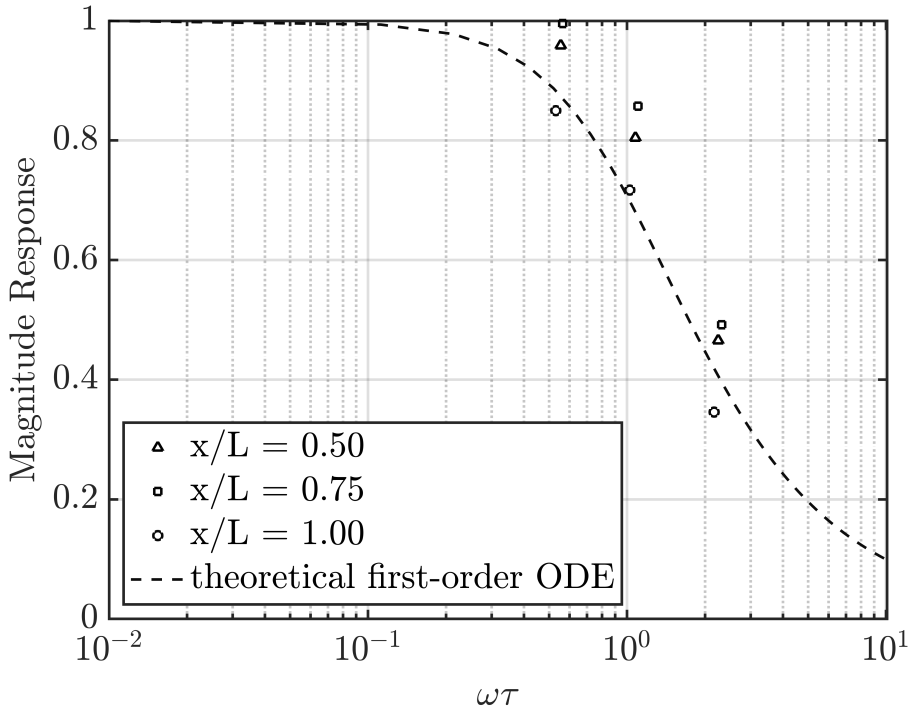

(a) Frequency response at various downstream distances. The data reasonably collapses to the theoretical fit (dashed line) $M = B/A = \sqrt{1 + \omega^2\tau^2}$ when L_t = 14.5 m according to eq. (2.13).

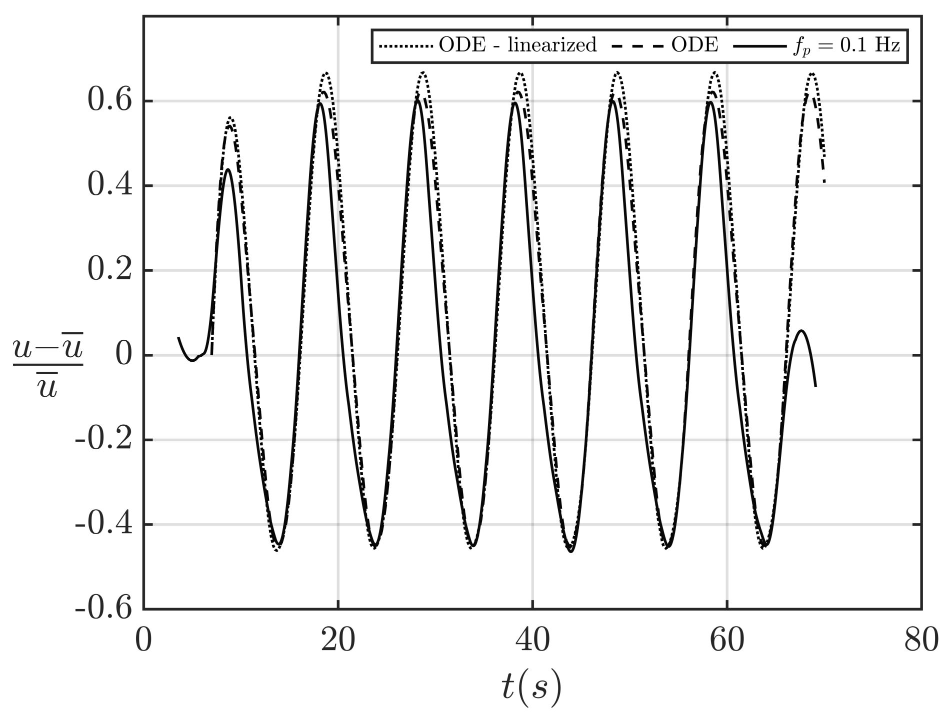

(b) Theoretical velocity time series solutions of eq. (2.12) with and without higher-order terms compared to experiment.

Figure 2.3: Response characteristics to sinusoidal forcing.

2.2 Types of flow generation

For a more detailed look into the types of flow generation possible in FAWT, the reader is referred to appendix A. Below briefly mentions some salient features worth bearing in mind for the upcoming analysis.

Flow Type #1: Steady, spatially-(non-)uniform

Using a custom-built 5-hole pressure probe and associated software both developed by Renn (2018), flow values can be spatially mapped in real time and further post-analyzed for select 2D slices of any measured steady flowfield, provided the spatial resolution is fine enough to promote reliable and accurate interpolated values. Each contour plot presented was interpolated with no greater than a thirty millimeter applicability radius. Flowfields 'painted' in this way give the viewer an intuitive view of the spatial distribution of the average velocity characteristics of a flowfield along planes of interest. For most cases, it is desirous to test far enough downstream so that the transient mixing behavior of each source fan mixes fully into a bulk flow. In a honeycomb-affixed-to-the-face-configuration, convergence of velocity and turbulence intensity along the centerline occurs beyond $x/L = 0.5$ (see fig. A.4). The near- and far-field flow evolution of a 3×3 ($d/L = 0.33$) dual-layer array is shown in fig. 2.4.

Selected views of a much larger and more finely-resolved 36×36 ($d/L = 0.03$) dual-layer array comprised of modules with distinct inlet geometry are given in fig. 2.5 and fig. 2.6. Unlike the open inlet design of fig. 2.4, a divergent geometry enclosing 3×3 fan units is placed upstream of the intake (see appendix B for more information). A selected mean velocity profile at $z/L = 0.3$ shows clearly a peaked behavior associated with the funneling influence of the module geometry. At $x/L = 0.35$, percentage deviation on average across the center portion of the array is 3.7% from the mean. The effect of the modules is still noticeable in visualizations at $x/L \sim 1.00$ (see fig. B.3), though the percentage deviation drops to 1.6%. Anything less than 2% is considered sufficiently uniform for the purposes herein. The variance in uniformity would be further reduced if a more traditional flow management system was installed (e.g. grids and screens). Similar treatment of the turbulence intensity distribution by hotwire traverses is given in fig. A.10. The nominal turbulence intensity values for a honeycomb only arrangement range between $\sim 3\% - 5\%$ in the regions of interest.

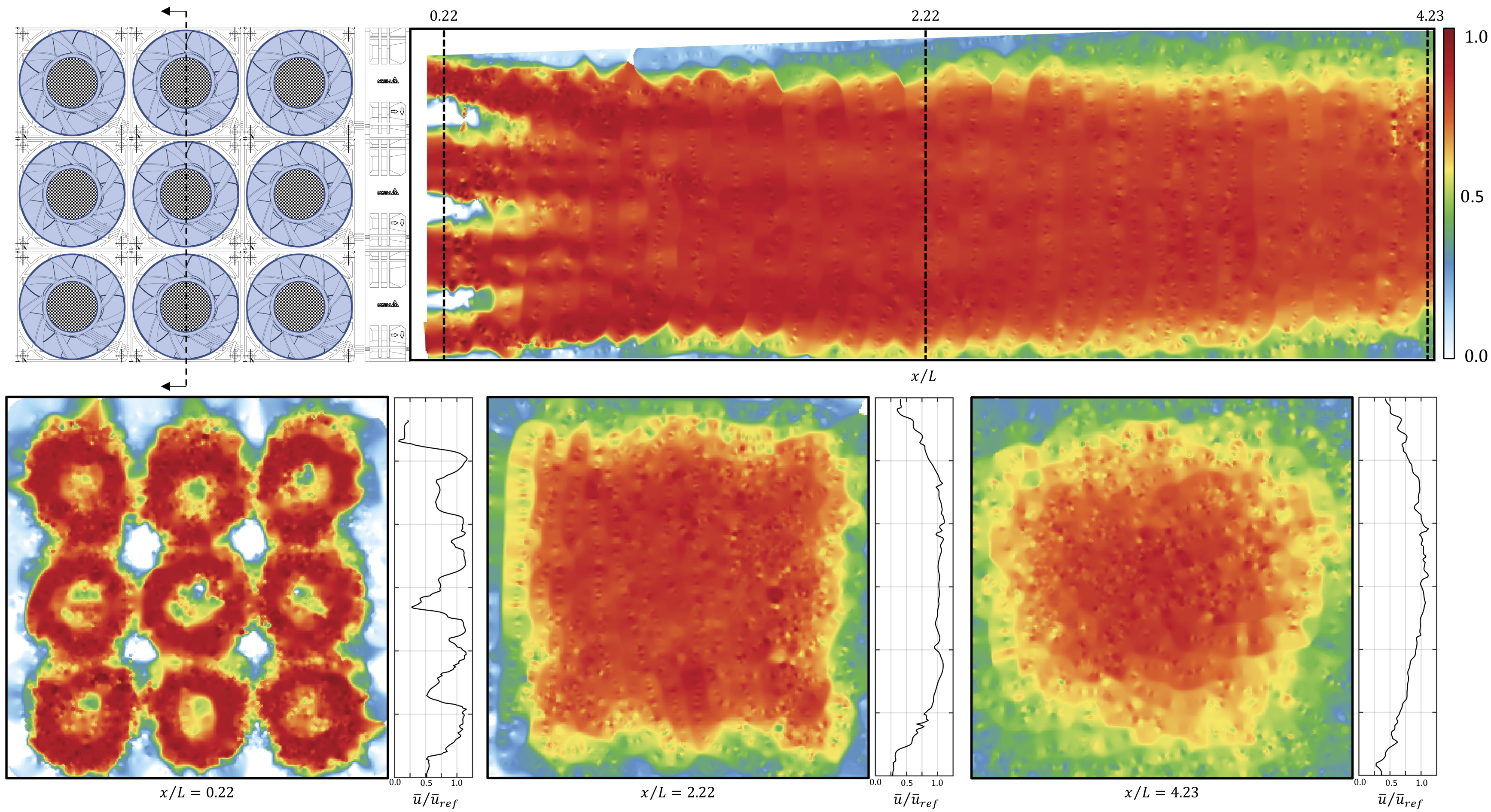

Figure 2.4: Development of a steady uniform flow measured for a $d/L = 0.33$ resolution dual-layer array ($d = 0.080$ m) with minimal mounting structure at fan unit intake. The streamwise (x-z plane) cut corresponds to the centerline plane ($y = 0$) and the positions of the spanwise (z-y plane) distributions are dashed for all three locations. To the right of each spanwise cut is a corresponding velocity profile at the centerline ($y = 0$) for that respective view. The core flow homogenizes first from discrete source units to a nearly uniform square cross section of size $L \times L$ and then spatially reduces with downstream distance as the core flow smoothes to a rounder cross-section as the boundary shear layers entrain and grow. The colorbar corresponds to $\overline{u}/\overline{u}_{max}$.

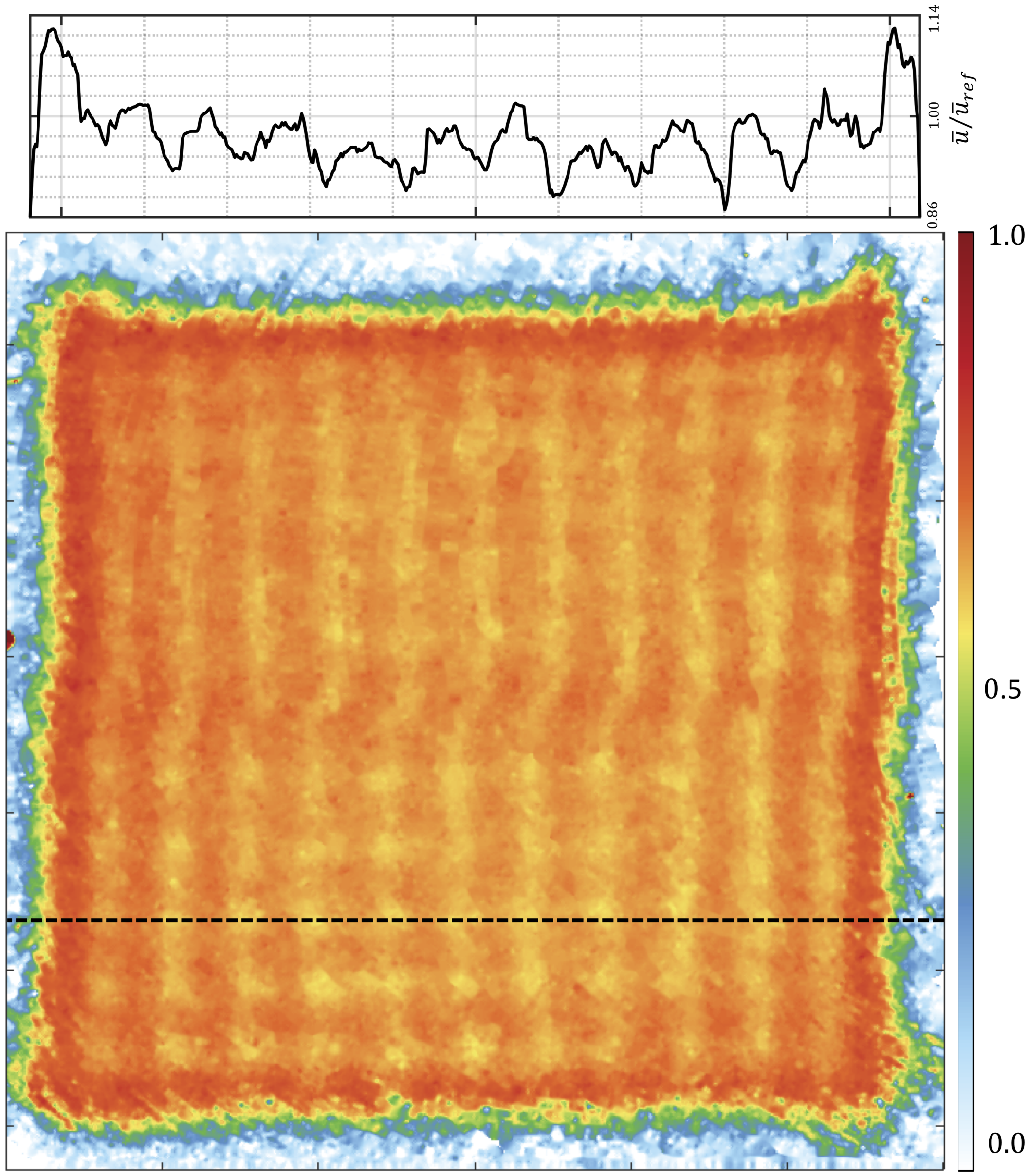

Figure 2.5: Spanwise (z-y plane) distribution of a steady uniform flow measured at the downstream location $x/L = 0.35$ for a $d/L = 0.03$ resolution dual-layer array. This particular fan array has outer dimensions $L = nd = 2.88$m ($n = 36$, $d = 0.080$ m) with $36 \times 36 \times 2 = 2592$ individual fan units stacked in two layers and arranged into 144 total modules. It is evident in this view that a funneling effect of the module geometry is still present. The dashed line corresponds to the location $z/L = 0.3$ of the extracted velocity profile above. The colorbar corresponds to $\overline{u}/\overline{u}_{max}$.

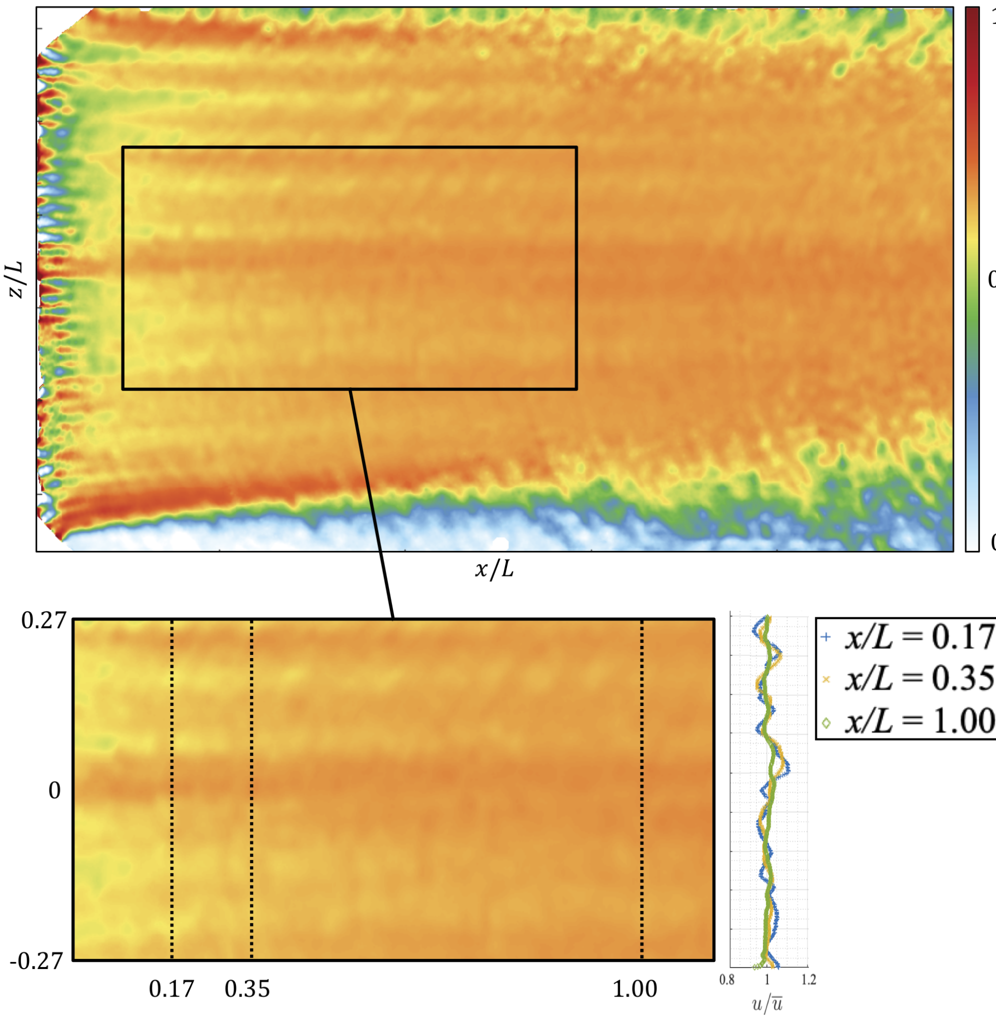

Figure 2.6: Streamwise (z-x plane) distribution along the centerline plane ($y = 0$) of a steady uniform flow for a $d/L = 0.03$ resolution dual-layer array. Velocity profiles in the middle portion of the array between $-0.27 < z/L < 0.27$ are extracted at three downstream locations $x/L = 0.17, 0.35$, and 1.00. The standard deviation of each profile is 3.6%, 2.9%, and 1.3%, respectively. The colorbar corresponds to $\overline{u}/\overline{u}_{max}$.

Both uniformity and turbulence statistics converge to a quasi-steady state when measured far enough downstream. The initial fan conditions are washed out in the natural evolution of the steady, spatially-uniform flow modality starting beyond $x/L \sim 0.2$. Though the effect of each module is felt for some distance further downstream, acceptable levels of uniformity are generally found near $x/L \sim 0.5$ and beyond.

Flow Type #2: Unsteady, spatially-(non-)uniform

The discrete and individual addressing of each fan unit enables both unsteady non-uniform and uniform flow configurations. When addressed uniformly in space but varying in time as in fig. 2.7, an unsteady gust flowfield can straightforwardly be measured by standard hotwire or pitot techniques. Below is one such experimental simulation of an instantaneous unsteady velocity profile.

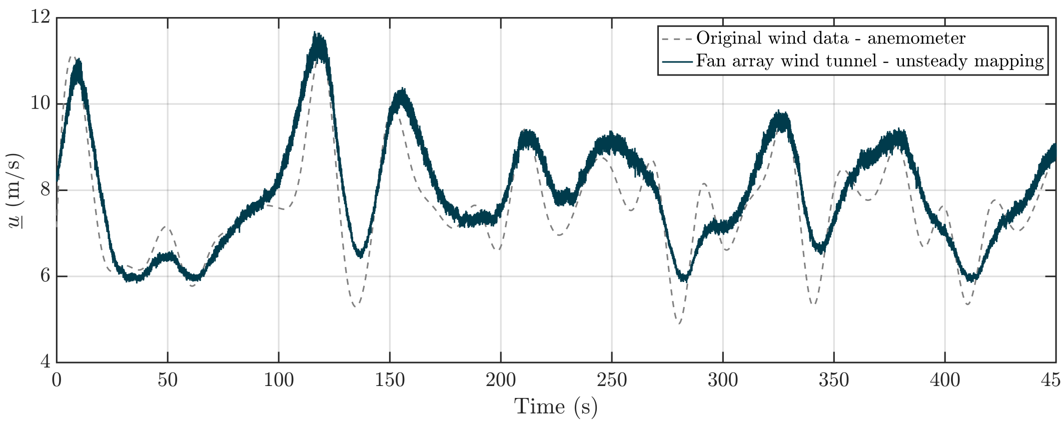

Figure 2.7: A velocity trace from a handheld wind anemometer recording of an instantaneous prevailing wind of a small uninhabited island in the Caribbean is mapped into the FAWT software environment to generate an input distribution that attempts to playback the simulated output. Prevailing winds in the region are directional and constant, averaging to be $8 - 10$ m/s at all times of the year, but their instantaneous nature is gusty, fluctuating as high as 11.5 m/s and as low as 2.5 m/s.

When coupled so as not to allow any phasing between adjacent fan units, a 'breathing' modality of the fan array is enabled. Continuously random gusts targeting a particular frequency introduce energy at a specific wavelength. Targeting particular frequencies in a gusty environment experienced globally by the flyer is accomplished by selecting forcing frequencies within the range $0.1 < f_p < 0.5$ Hz while implemented in the 'breathing' modality. Amplitudunal response of the commanded input to expected output would behave according to the frequency bandwidth of the particular fan array used (see section 2.1). Measured real-world instantaneous velocity records can be mapped and simulated reproducibly by comparing the output to the original and iterated upon until satisfactory results are rendered, within the constraints of the system itself.

Flow Type #3: Quasi-steady irrotational sinusoidal

It was shown in fig. 2.3 that responses to sinusoidal inputs are sinusoidal outputs at a phase delay, with magnitude approximately determined by $\sqrt{1+\omega^2\tau^2}$. Where periodic external forcing is expected to play an important role, a useful alternative expression is to triply decompose the flowfield as:

$$\underline{u} = \overline{u} + u^{\nsim} = \overline{u} + u' + \tilde{u} \tag{2.15}$$

where u' represents the fluctuating component (i.e. background turbulence) and $\tilde{u}$ is the forced periodic component. This is an all-encompassing prescription, particularly useful for cyclic unsteady flows.

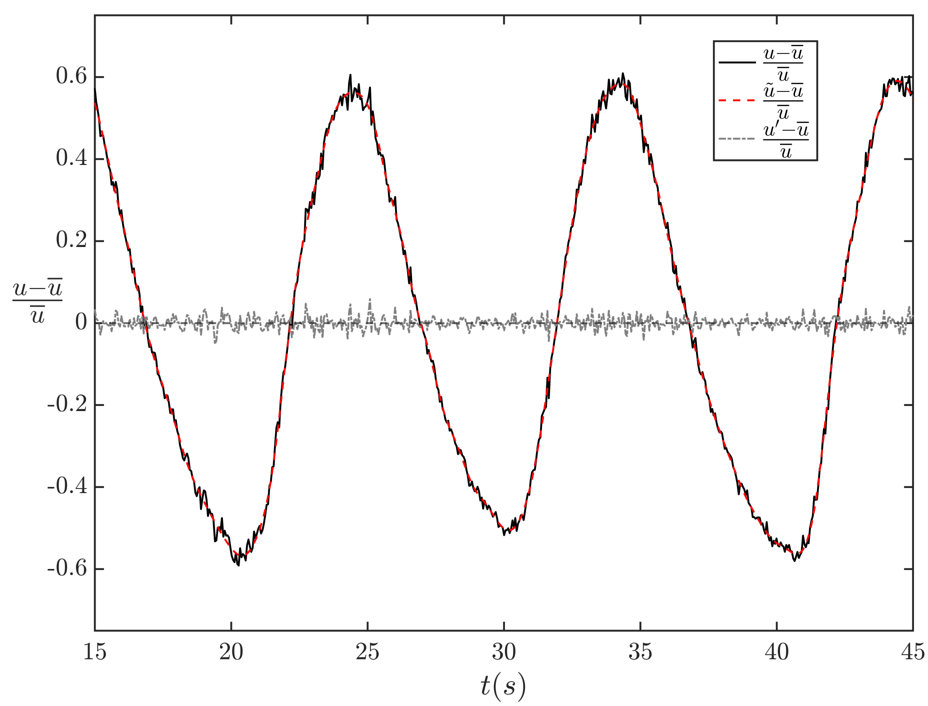

Figure 2.8: Example analyses afforded by the triple decomposition. Filtering out the forced frequency ($f_p = 0.1$ Hz) periodic sinusoidal portion of the signal $\tilde{u}$ isolates the stochastic fluctuating content u'.

2.3 Summary

A mathematical framework applied to a typical source fan unit of outer dimension d with flow emanating from an annular area output A_{ann} was first introduced. Through fundamental treatment of the conservation of momentum for an incompressible, irrotational, inviscid, non-steady, constant density flowfield in the absence of a changing external body force, an unsteady form of Bernoulli's equation along a streamline is derived (eq. (2.4)). Through further consideration of the continuity equation, eq. (2.4) is recast in the more readily accessible test section freestream velocity u_∞ as a function, ultimately, of manufacturer provided source-fan performance input specifications and expanded to $n-$fan units without loss of generality for the uniform steady and 'breathing' quasi-steady flow modalities. The theoretical response to a purely oscillatory forcing function input of the 'breathing' modality is then considered and the frequency response of the flowfield (beyond the initial mixing region) was determined to behave as a low-pass filter with air moving as a phase-delayed lumped mass (fig. 2.3). Next, extensive flow visualizations of the streamwise and transverse development of the baseline steady uniform flow modality is presented, first for a $d/L = 0.33$ array (the typical 'benchtop' size array) in fig. 2.4 and then for the full-size $d/L = 0.03$ array (used predominantly throughout the rest of the dissertation) in fig. 2.5 and fig. 2.6. Finally a brief discussion of unsteady gust flowfield generation is given and an all-encompassing triple decomposition that better accounts for the, at times, discrete periodic component of flowfield generation (used extensively in perturbation techniques) is introduced in eq. (2.15).